Last interglacial sea-level oscillations

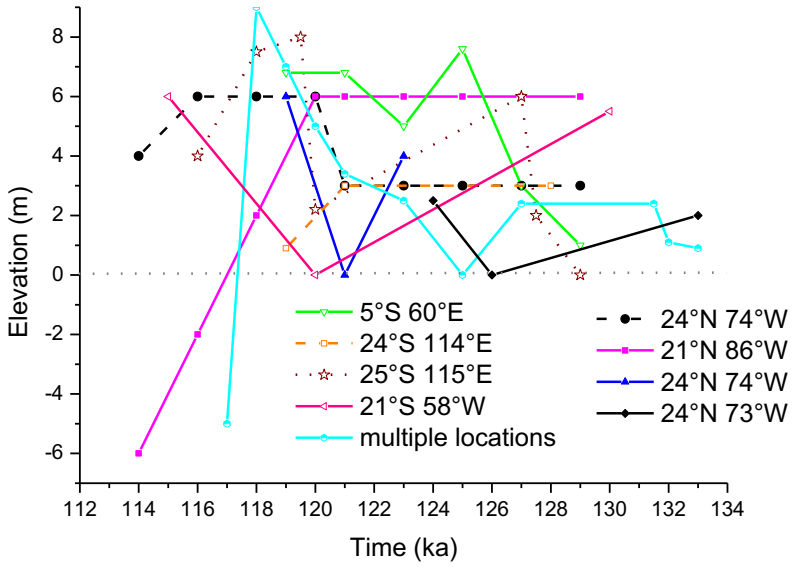

Fig. S1. LIG sea-level oscillations inferred from various sites. North hemisphere (reef-based) sites are Bahamas (24°N 74°W; Chen et al., 1991; Wilson et al., 1998; Thomson et al., 2011) and Yucatan peninsula (21°N 86°W; Blanchon et al., 2009); South hemisphere (reef-based) sites are Seychelles (5°S 60°E; Dutton et al., 2015), Hawaii (21°S 58°W; Sherman et al., 1993) and Western Australia (24°S 114°E; Stirling et al., 1998; O'Leary et al., 2013). Multiple locations (Hearty et al., 2007) include Bermuda, Barbados, Bahamas, Hawaii, W-Australia, and the non-reef site in the Mediterranean. The Red Sea record is not presented here because the sea-level estimates derived from the oxygen isotope record describe sea-level oscillations that are greater than 12 m (Siddall et al., 2004). For the sake of clarity no error bars are depicted.

The Hergla Site

Previous studies: The site was studied by Herm et al. (1980), Paskoff and Sanlaville (1983), Mahmoudi (1986), Jedoui et al. (1987), Hearty (1986), Richards (1986), Wood (1994), Le Guern (2004), Le Guern and Davaud (2005). While Harms et al (1980) and Mahmoudi (1986) were largely descriptive in their approach, Paskoff and Sanlaville (1983) interpreted the site in terms of their concept of stratigraphic formations or members being genetically linked to climate events. Jedoui et al. (1987), Hearty (1986), Richards (1986) and Woods (1984) focused on dating selected parts of the cliff section where the work of Hearty (1986) was most influential due to the, then, innovative approach of developing an amino-acid

racemisation (AAR) stratigraphy calibrated to U/Th ages, by which many late Quaternary deposits were dated for the first time. Le Guern (2004) and Le Guern and Davaud (2005) focused on the sedimentology of single outcrops within the elongated cliff. The latter authors described details of the succession of coastal facies and our description is very similar to theirs.

The facies succession: Logs and facies correlation of the central part of the cliff are shown in Fig. S2. Our interpretation in terms of a depositional model is shown below the logs in Fig. S2. The main section, indicated with a hammer in Fig. S2 was investigated in all previous studies. Its succession is shown in Fig. 3 (main text).

The surfaces: according to Hearty et al. (2007) the top of the lower aeolian deposit is a "weathering surface" and is associated with a sea level "fall to near or below present level (0 m)" (Hearty et al., 2007, p. 2099). In our correlation panel the aeolian deposit is in juxtaposition to the lagoonal deposit suggesting the shoreline was situated seaward at an unknown distance to the dune. The dune's top is a buried subaerial surface that is spatially limited to the central and northern part of the cliff where the exposure of the bay to the northeast allowed aeolian sand to accumulate.

The cobble beds: All cobbles and boulders are moderately to well rounded with elongated a-axes. They are made of local foreshore and shoreface material (i.e. total absence of foreign material) and mixed with mollusc shell fragments. We identify 2 beds in stratigraphically different positions, both laterally limited to the cliff section. The first cobble layer (modelled time of deposition 87±10 ka) overlies the lagoonal deposits and the shoulder of the Pliocene headland. The second cobble layer mainly affected the central part of the barrier at ~67 ka. Two high energy events seem to have occurred for yet to establish reasons. We assume fracturing of the inner shelf deposits during an earthquake, subsequent reworking of the debris in the swash zone and finally transport of cobbles and boulders by storm onto the barrier.

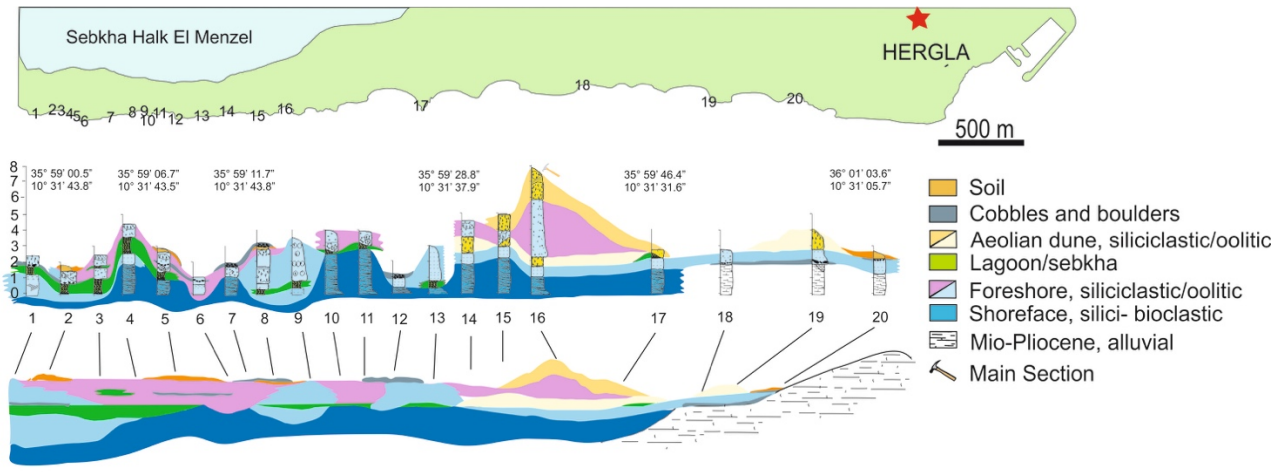

Fig. S2. Topographic map of the cliff with numbers of logs; logs and correlation of facies; depositional model deduced from logs.

Sediment analysis

Texture, composition and matrix properties were identified from thin sections and carbonate mineralogy was studied using cathodoluminescence. Facies interpretation was based on a combination of sediment components, texture, matrix and bedding structures following standard criteria for carbonate and clastic petrographic sediment analysis (Dunham, 1962; Pettijohn et al., 1972; Flügel, 2004). No geochemical analyses were carried out because thin section analysis revealed dissolution of the oolitic aragonite and precipitation of equant sparry calcite cements typical of meteoric diagenesis.

Sea-level index point (SLIP) analysis

Here the top of the lagoon and the midpoint of the upper foreshore deposits, an average tidal range of 0.3±0.2 m and the square-root rule for error calculation are used for SLIP analysis (see Fig. S3 for concept): the lagoon top with a modelled age of 110±15 ka represents the corresponding palaeo-shoreline situated at 3.0±0.5 m. The midpoint of the upper foreshore with a modelled age of 86±4 ka is situated at 4±2 m. Assuming an average foreshore water depth of 3±3 m the corresponding palaeo-shoreline is situated at 7±3 m. Thus, at Hergla the MIS 5e shoreline is today situated several meters below and the MIS 5a shoreline several meters above the inferred global level of the respective time interval (e.g., Lambeck and Chappell, 2001). While the local processes leading to these displacements are yet to be studied, it is clear that the Hergla site is not suitable for sea-level studies.

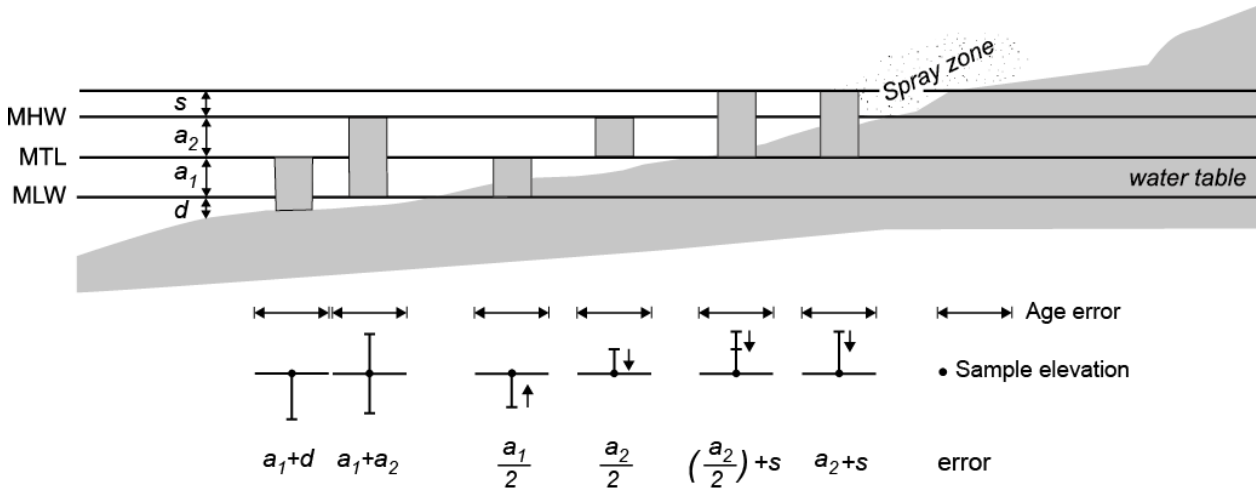

Fig. S3. Illustration of indicative range of a foreshore deposit and associated error. The indicative range spans from upper shoreface to spray zone encompassing the range from mean low water level (MLW) to mean high water level (MHL). Following Shennan et al. (2015) the midpoint of each zone is the reference water level. The minimum vertical error is half the tidal amplitude (a / 2) and the maximum error is the tidal range (a1+a2). Tidal amplitude is half of the tidal range; a1=tidal amplitude between MTL and MLW; a2=tidal amplitude between MTL and MHW; d=maximum water depth of foreshore formation zone; s = elevation of the spray zone (Mauz et al., 2015).

Optical Dating

Samples were obtained by breaking off large blocks of cemented sediment from the section. In the laboratory, preparation and measurements followed standard procedures and protocols (e.g., Mauz et al., 2002); Data analysis and modelling followed Mauz et al. (2009) where aliquots exhibiting a characteristic saturation dose value below a certain threshold (i.e. D_0<47 Gy) were rejected. To assess potential age underestimation caused by variable saturation doses of natural sedimentary quartz the standard dose-recovery protocol was employed with given doses of 60 Gy to 130 Gy in steps of 30 Gy using 6 aliquots per dose step. A statistically significant trend towards underestimation was observed for doses of 100 Gy and beyond (Fig. S4). Because natural doses between 30 Gy and 70 Gy were determined (see D_e in Table S2), age underestimation is thought to be negligible.

The relatively broad dose distribution (see σ, % in Table S1) is thought to be the result of the time-dependent change of the radiation field in the sample due to the ingrowth of secondary carbonate in

the pore space between sediment components. This secondary carbonate has energy absorption coefficients that differ from air or water and so, for instance, the range of 1 MeV electrons is around half of what it would be in water. As a result, radiation from hotspots reach a smaller volume of detrital components when carbonate covers the pore space instead of water or air. It is therefore likely that the dispersion of D_e values increase with increasing carbonate content. To account for the time-dependence of the the dose rate, the *Carb* model (Mauz and Hoffmann, 2014) constructs as a series of values where the water content is proportionately reduced until it reaches a new constant level. The age of the sample is estimated as the length of time needed for the integrated dose rate to equal the D_e value. Multiple Bayesian runs (see below) identified the age of sample LV636 to be overestimated. This can be explained by the fact that the quartz grains used for optical dating occurred as nucleus of ooids (Fig. S5) and were not reset when transported during the subsequent MIS 5a transgression.

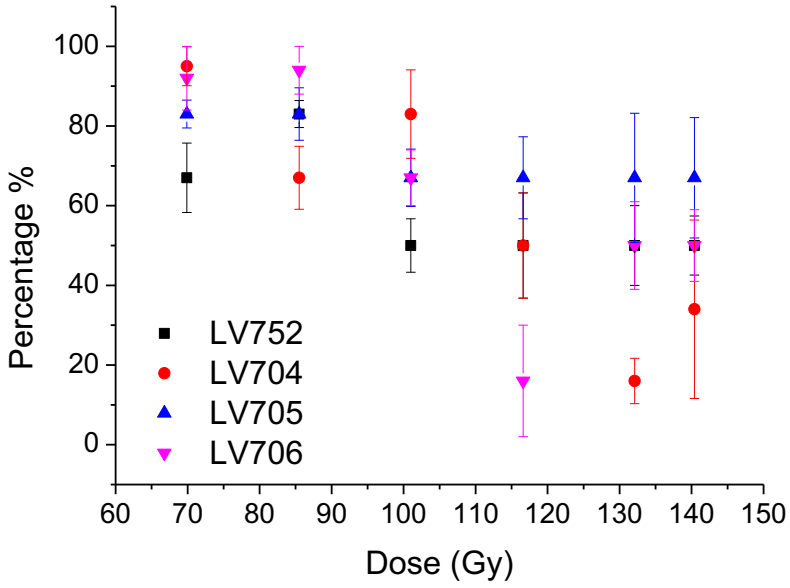

Fig. S4. Percentage of aliquots recovering the given dose within 10% of unity (before D_0<47 Gy rejection) in four different samples. The percentage decreases with increasing dose with a significant drop at around 100 Gy.

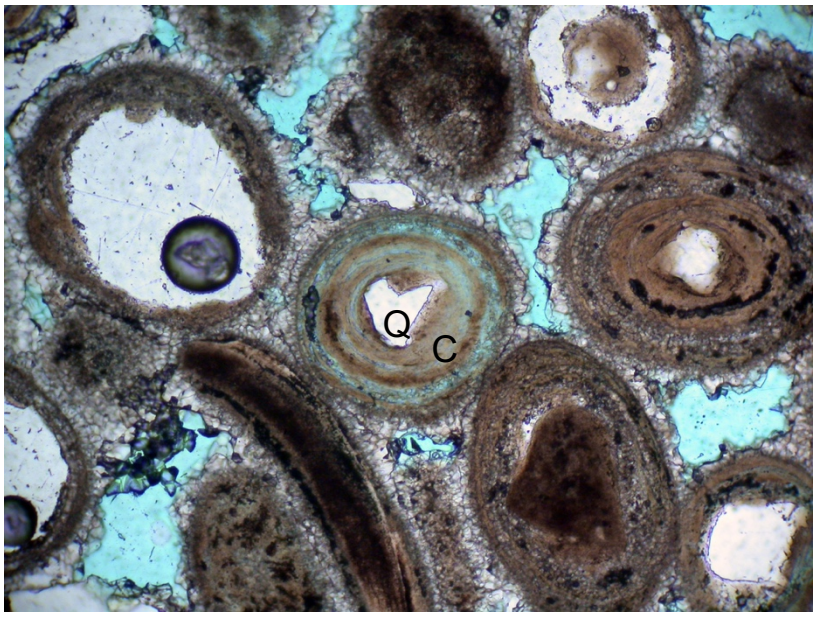

Fig. S5. Thin section image of the sample LV636. Quartz grains (Q) are enclosed by a micritic cortex (C) composed of concentric rings. Some of these rings are diagenetically altered, i.e. replaced by calcite crystals.

Table S1. Statistical parameters used to decide on the statistical model used for D_e estimation and D_e estimates. σ= over-dispersion, *c*=weighted skewness, *s*=skewness of lnDe, *k*=standardised kurtosis. Median statistics was used for D_e estimation to account for multi-grain OSL signals and to average out the secondary carbonate effect on the sedimentary radiation field.

Sample code (LV)	**Aliquot size (mm)**	**Aliquot# (accepted/ measured)**	**Descriptive Statistics**				**D_e (Gy; median, ±se)**
	3		***σ*(%)**	***c***	***s***	***k***	
635	3	31/72	22±2	1.11	1.71	1.53	45.7 ± 1.5
704	3	64/72	19±2	0.98	1.82	3.87	38.8 ± 1.1
705	3	48/72	24±3	1.07	2.00	3.27	33.8 ± 1.6
706	3	34/48	21±3	0.98	1.90	2.93	37.9 ± 1.3
678	3	41/48	35±2	-0.75	0.07	-0.51	32.9 ± 1.7
636	3	47/60	19±2	0.72	1.12	0.30	44.0 ± 1.4
707	3	54/60	27±3	0.74	2.24	6.18	66.9 ± 3.3

752	3	29/48	47±6	0.10	2.36	7.72		45.2 ± 1.8

Bayesian Analysis

OxCal uses a Markov chain Monte-Carlo (MCMC) algorithm to combine the OSL ages (each age is a *likelihood* that is a probability distribution representing the measured age and its uncertainty) and the stratigraphic order of the OSL samples (*prior*) to produce age estimates (each age estimate is a *posterior* that is a probability distribution representing the modelled age and its uncertainty) of both the OSL samples and key stratigraphic boundary (Bronk Ramsey, 2009). In simple, the program generates one age-sequence combination each time by randomly taking one sample from each *likelihood* and repeating this iteration millions of times to exhaust all possible combinations. After rejecting combinations contracting the *prior*, the other combinations are used to produce the *posterior* for each sample and stratigraphic boundaries. The Agreement Index is calculated for each sample and for the whole model to evaluate confidence of the modelling results, where a value >60% corresponds to about >95% probability of a chi-squared distribution (Bronk Ramsey and Lee, 2013). The code used to run the model without LV636 is detailed below:

```
Plot()
 {
  Sequence("Hergla")
  {
   Boundary("Bottom");
   Age("LV635",N(109040,4000));
   Age("LV704",N(119040,5000));
   Boundary("SB2_start");
   Interval_SB2();
   Boundary("SB2_end");
   Age("LV705",N(91940,5000));
   Age("LV706",N(90940,4000));
   Age("LV752",N(82940,5000));
   Boundary("SB1_start");
   Interval_SB1();
   Boundary("SB1_end");
```

```
  Age("LV678",N(66940,3000));
  Age("LV707",N(57940,3000));
  Boundary("Top");
 };
};
```

Table S2. Sediment facies of dated samples and analytical data of radioactive elements and cosmic dose rate used for OSL age estimation. Ages are *Carb* ages (Mauz and Hoffmann, 2014) with assumed internal dose of 0.01±0.005 Gy/ka (Vandenberghe et al., 2008).

Sample Code	Sediment Facies	Water content (%)	Grain Size (µm)	U (µg g^{-1})	Th (µg g^{-1})	K (wt %)	$\dot{D}_{cosm}$ (Gy ka^{-1})	$\dot{D}_{final}$ (Gy ka^{-1})	Age (±1σ, ka)
635	shoreface	5±1	275±50	1.05±0.03	0.597±0.006	0.083±0.009	0.063±0.003	0.42±0.01	110±4
704	foreshore	5±1	275±50	0.58±0.02	0.62±0.06	0.064±0.008	0.119±0.006	0.32±0.01	120±5
705	foredune	5±1	275±50	0.56±0.02	0.61±0.06	0.110±0.008	0.095±0.005	0.37±0.01	92±5
706	foredune	5±1	275±50	0.70±0.02	0.95±0.06	0.081±0.009	0.121±0.006	0.43±0.01	91±4
678	beach	5±1	275±50	0.70±0.02	0.76±0.05	0.095±0.006	0.194±0.009	0.50±0.01	67±3
636	foreshore	5±1	275±50	0.80±0.02	0.78±0.06	0.054±0.008	0.124±0.006	0.41±0.01	106±3
707	dune	5±1	275±50	2.11±0.05	7.24±0.15	0.059±0.009	0.1373±0.007	1.25±0.02	58±3
752	beach	5±1	225±75	1.24±0.03	0.54±0.05	0.04±0.008	0.1566±0.008	0.52±0.008	86±4

Table S3. Summary of Bayesian modelling result for OSL samples from the Hergla site. For graphical display of data see Fig S6.

Amodel=65.4%	Unmodelled (BP)						Modelled (BP)					
	from	to	%	from	to	%	from	to	%	from	to	%

Top Boundary							62630	52150	68.1	65849	39185	95.4
LV707 Year-N(57940,3000)	61000	54880	68.2	63940	51940	95.4	63040	57040	68.2	65590	53920	95.4
LV678 Year-N(66940,3000)	70000	63880	68.2	72940	60940	95.4	68320	62560	68.2	71350	60070	95.4
SB1_end Boundary							74242	63612	68.2	82546	60996	95.4
SB1_start Boundary							88592	77690	68.2	91832	70200	95.4
LV752 Year-N(82940,5000)	88040	77840	68.2	92940	72940	95.4	89690	82190	68.2	92690	77740	95.4
LV706 Year-N(90940,4000)	95020	86860	68.2	98940	82940	95.4	92260	86380	68.2	95260	83460	95.4
LV705 Year-N(91940,5000)	97040	86840	68.2	101940	81940	95.4	95340	88390	68.2	99290	85390	95.4
SB2_end Boundary							99989	89332	68.1	107495	86221	95.4
SB2_start Boundary							113963	104646	68.2	117364	97004	95.4
LV704 Year-N(119040,5000)	124141	113941	68.2	129041	109041	95.4	114741	108091	68.2	117991	104791	95.4
LV635 Year-N(109040,4000)	113121	104961	68.2	117041	101040	95.4	116041	109481	68.2	119361	106241	95.4
Bottom Boundary							118946	109966	68.1	128257	105813	95.4

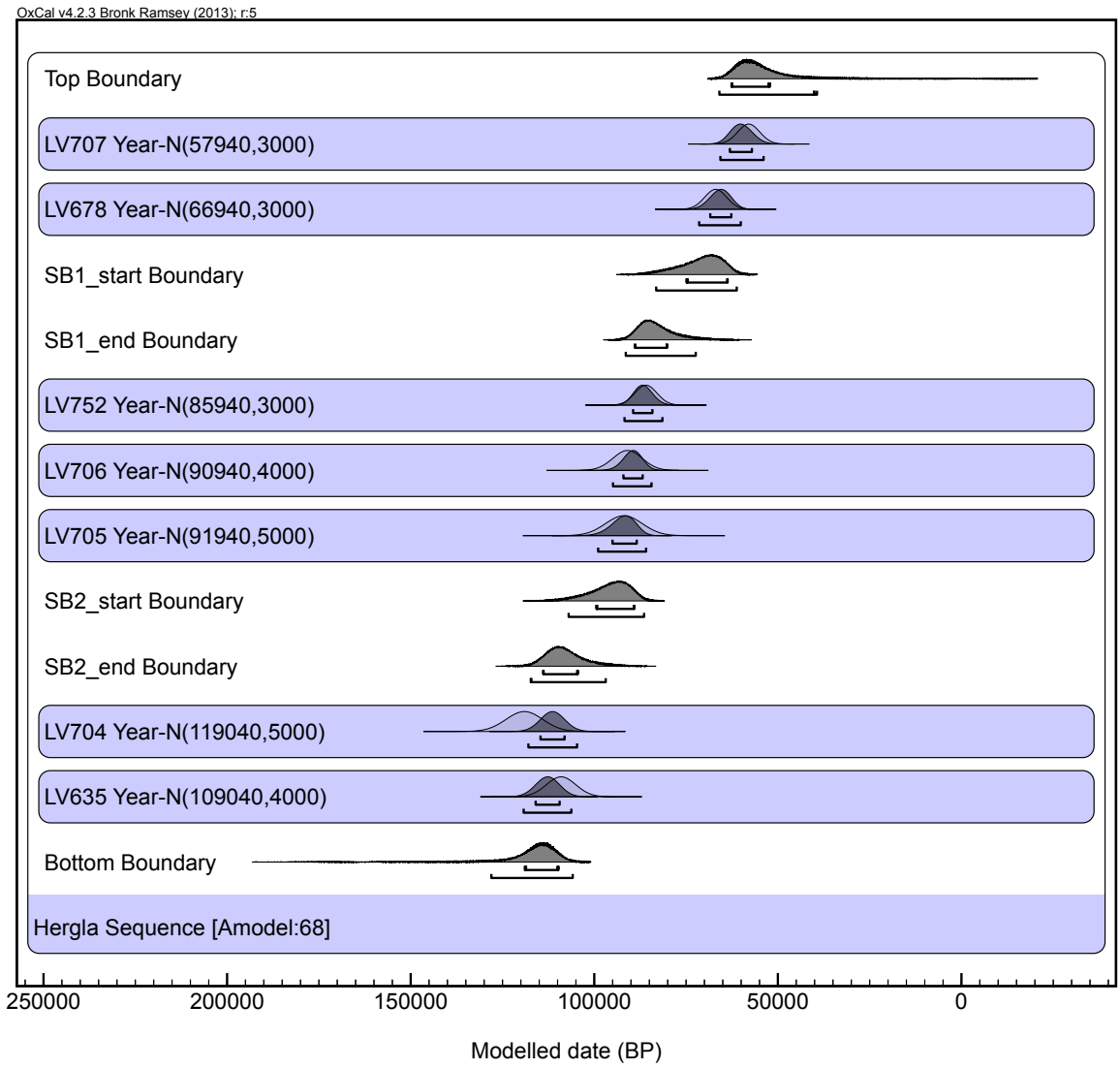
OxCal v4.2.3 Bronk Ramsey (2013); r:5
Top Boundary
LV707 Year-N(57940,3000)
LV678 Year-N(66940,3000)
SB1_start Boundary
SB1_end Boundary
LV752 Year-N(85940,3000)
LV706 Year-N(90940,4000)
LV705 Year-N(91940,5000)
SB2_start Boundary
SB2_end Boundary
LV704 Year-N(119040,5000)
LV635 Year-N(109040,4000)
Bottom Boundary
Hergla Sequence [Amodel:68]
250000
200000
150000
100000
50000
0
Modelled date (BP)

Fig. S6. Bayesian modelling result for OSL samples from the Hergla site.

References

Bronk Ramsey, C. 2009. Bayesian analysis of radiocarbon dates. *Radiocarbon* 51, 337–60

Bronk Ramsey, C., and Lee, S., 2013. Recent and planned developments of the program OxCal: *Radiocarbon*, 55, 720-73.

Dunham, R.J., 1962. Classification of carbonate rocks according to depositional texture. *American Association of Petroleum Geologist* Memoir 1, 108-121.

Flügel, E., 2004. Microfacies of carbonate rocks. Springer Berlin Heidelberg.

Hearty, P.J., 1986. An inventory of Last Interglacial (sensu lato) age deposits from the Mediterranean Basin: a study of isoleucine epimerisation and U-series dating. *Zeitschrift Geomorph. N.F.Suppl.-Bd*. 62, 51–69.

Herm, D., Paskoff, R., Sanlaville, P., 1980. La stratigraphie des falaises d'Hergla (Sahel del Sousse, Tunisie) et son importance pour la comprehension du Quaternarire marin recent de la Tunisie. *Comptes Rendus Sommaire de Societe Geologique Francaise* 1, 25–28.

Jedoui, Y., Davaud, E., Strasser, A., 1987. Sédimentation et diagenèse du cordon littoral Tyrrhénien de la Sebkha Halk el Menzel (Hergla, Tunisie). *Notes du Service Géologique de Tunisie*, 55, 46–74.

Le Guern, P., 2004. Caractérisation pétrographique et prétexturale des éolianites holocènes et pléistocènes. Thèse 3e cycle Sciences de la Terre, Université de Genève, 219 p.

Le Guern, P., Davaud, E., 2005. Recognition of ancient carbonate wind deposits: lessons from a modern analogue, Chrissi Island, Crete. *Sedimentology* 52, 915–926.

Mahmoudi, M., 1986. Stratigraphie, sédimentologie et diagenèse des dépôts tyrrhéniens du Sahel tunisien (Tunisie orientale). Thèse Université Paris sud, Orsay, 323 p.

Mauz, B., Vacchi, M, Green, A., Hoffmann, G. and Cooper, A., 2015. Beachrock: A tool for reconstructing relative sea level in the far-field. *Marine Geology* 362, 1-16.

Mauz, B. and Hoffmann, D., 2014. What to do when carbonate replaced water: *Carb*, the carbonate dose-rate model for estimating dose rates. *Ancient TL* 32, 24-32.

Mauz, B., Bode, T., Mainz, E., Blanchard, H., Hilger, W., Dikau, R. and Zöller, L., 2002. The luminescence dating laboratory at the University of Bonn: Equipment and procedures. *Ancient TL*, 20, 53-61.

Mauz, B., Elmejdoub, N., Nathan, R. and Jedoui, Y., 2009. Last interglacial coastal environments in the Mediterranean-Sahara transition zone. *Palaeogeography, Palaeoclimatology, Palaeoecology* 279, 137-146.

Paskoff, R., Sanlaville, P., 1983. Les côtes de la Tunisie: Variations du niveau marin depuis le Tyrrhénien. Editions Maison de l'Orient, Lyon, France, p. 192.

Pettijohn, F.J., Potter, P.E., Siever, R., 1972. Sand and Sandstone. Berlin, Heidelberg New York, p. 426.

Richards, G.W., 1986. Late Quaternary deformed shorelines in Tunisia. *Zeitschrift Geomorph. N.F., Suppl.-Bd.* 62, 183-168.

Siddall, M., Smeed, D.A., Hemleben, C., Rohling, E.J., Schmelzer, I. and Peltier, W.R., 2004. Understanding the Red Sea response to sea level. *Earth and Planetary Science Letters* 225, 421– 434.

Shen, Z. and Mauz, B., 2011. Estimating the equivalent dose of late Pleistocene fine silt quartz from the Lower Mississippi Valley using a common OSL growth curve. *Radiation Measurements* 46, 649-654.

Shennan, I., 2015. Handbook of sea-level research: framing research questions, in: Shennan, I., Long, A.J. and Horton, B.P. (eds)., Handbook of sea-level research, Wiley, pp.3-25.

Sherman, C.E., Glenn, C.R., Jones, A.T., Burnett, W.C. and Schwarcz, H.P., 1993. New evidence for two highstands of the sea during the last interglacial, oxygen isotope substage 5e. *Geology* 21, 1079-1082.

Vandenberghe, D., De Corte, F., Buylaert, J.-P., Kučera, J. and Van den haute, P., 2008. On the internal radioactivity in quartz. *Radiation Measurements* 43, 771-775.

Wilson, M.A., Curran, H.A. and White, B., 1998. Paleontological evidence of a brief global sea-level event during the last interglacial. *Lethaia* 31, 241-250.

Wood, P.B., 1994. Optically stimulated luminescence dating of a late Quaternary shoreline deposit, Tunisia. *Quaternary Science Reviews* 13, 513–516.